Electronic Supplementary Material (ESI) for Journal of Materials Chemistry B.

Surface Nanocrystallization Enhances Biomedical Performance of Additively Manufactured Stainless Steel

Sumit Ghosh[1#], Sushma Indrakumar[1], Santanu Ghosh[1], Vasanth Gopal[2], Sagar Nilawar[1], Geetha Manivasagam[2], Jayanth S. Kesave[3], Satyam Suwas[1], Kaushik Chatterjee[1*]

[1]Department of Materials Engineering, Indian Institute of Science, Bangalore, Karnataka, India

[2]Centre for Biomaterials, Cellular and Molecular Theranostics, Vellore Institute of Technology, Vellore, Tamil Nadu, India

[3]Cranio Maxillofacial Surgery, Narayana Hospital, HSR Layout, Bangalore, Karnataka, India.

[*]Corresponding author:

Email: kchatterjee@iisc.ac.in

Phone: +91-80-2293-3408

Fax: +91-80-2360-0472

[#]Current address:

Materials and Mechanical Engineering, Centre for Advanced Steels Research, University of Oulu, 90014, Finland.

Abstract

Additive manufacturing enables the fabrication of patient-specific implants of complex geometries. Although selective laser melting (SLM) of 316L stainless steel (SS) is well established, post-processing is essential to preparing high-performance biomedical implants. The goal of this study was to investigate surface mechanical attrition treatment (SMAT) as a means to enhance the electrochemical, biomechanical, and biological performances of 316L SS fabricated by SLM in devices for the repair of bone tissues. SMAT conditions were optimized to induce surface nanocrystallization on the additively manufactured samples. SMAT resulted in a thicker oxide layer, which provided corrosion resistance by forming a passive layer. The fretting wear results showed that the rate of wear decreased after SMAT owing to the formation of a harder nanostructured layer. Surface modification of the alloy by SMAT enhanced its ability to support the attachment and proliferation of pre-osteoblasts *in vitro*. The study of the response *in vivo* to the additively manufactured alloy in a critical-sized cranial defect murine model revealed enhanced interactions with the cellular components after the alloy was subjected to SMAT without inducing any adverse immune response. Taken together, the results of this work establish SMAT of additively manufactured metallic implants as an effective strategy for engineering next-generation, high-performance medical devices for orthopedics and craniomaxillofacial applications.

Keywords: Nanocrystals; Potentiodynamic polarization; Fretting wear; Biomaterials

1. Introduction

The demand for high-performance metallic implants is rapidly increasing worldwide to treat orthopedic, oral, cranial, and maxillofacial disorders that arise due to disease, trauma, or congenital defects. 316L stainless steel (SS) is a well-established metallic biomaterial widely used for preparing clinical-grade implants owing to its good mechanical properties, corrosion resistance, and biocompatibility.[1,2] Apart from 316L SS, other alloys, such as Co-Cr alloys and Ti-6Al-4V, have wide applications in the biomedical device industry due to their excellent mechanical properties, corrosion resistance, and biocompatibility.[3] These alloys are also used for preparing orthopedic implants. Additive manufacturing techniques involve the layer-by-layer fabrication of materials, often by melting using a laser or an electron beam. Selective laser melting (SLM) is the most widely used metal AM technique to produce near-net-shape components of complex geometry with high dimensional accuracy.[4] However, other techniques, such as electron beam melting, directed energy deposition, etc., are also being developed. In recent years, novel Ti-Nb, Ti-Nb-Zr, and other β-Ti alloys are being actively researched to develop alloys of low elastic modulus for minimizing stress shielding while incorporating non-toxic alloying elements.[5–7] Most recently, some of these alloys have been processed by additive manufacturing.[8] Despite their promise, they are yet to be widely adopted for manufacturing implants in the clinic. 316L SS continues to be popular in view of its corrosion resistance, cost-effectiveness, ease of manufacturing, and established history as an orthopedic biomaterial.

Conventional manufacturing processes require extensive machining to shape the final product, leading to high material wastage. The fabrication of complex parts is challenging and time-consuming. Mass-produced parts suffer from poor anatomical fit, compromising clinical outcomes. Recent advancements in AM / three-dimensional (3D) printing technologies can

overcome the limitations of traditional approaches. They afford the possibility of fabricating complex structures and personalized bone implants designed using magnetic resonance imaging (MRI) or computed tomography (CT) images of the patient's defect sites.[9,10] Additive manufacturing techniques involve the layer-by-layer melting of materials using a laser or an electron beam. SLM is the most widely adopted additive manufacturing technique used to produce near-net-shape implants of complex geometry with high dimensional accuracy.[11] Fabrication of 316L austenitic SS is now well established to prepare parts with good consolidation and minimal defects.[10,12,13]

However, there is significant scope for improving the performance of the as-manufactured devices for better clinical outcomes. Due to a surge in the use of implants in younger patients and an increase in the average human life expectancy, metallic implants are required to have an improved lifetime. The implants fail due to various surface-dependent phenomena, namely, corrosion, wear, and poor osseointegration.[14,15] Moreover, it is reported that 316L SS prepared by SLM has less favorable fatigue performance than its conventionally manufactured counterparts due to inherent defects, tensile residual stress, and rough surface. These drawbacks significantly limit the application of the as-manufactured parts in demanding applications. Therefore, effective surface engineering of the as-manufactured parts is critical to developing the next-generation orthopedic, oral, cranial, and maxillofacial implants. Reports suggest that nanocrystalline metallic surfaces can improve corrosion resistance and mechanical properties. Additionally, nanocrystalline metallic surfaces enhance cell attachment, osteoblastic differentiation, and osseointegration. A nanocrystalline surface can be generated either by a bulk severe plastic deformation (SPD) process, namely, equal channel angular pressing (ECAP), high-pressure

torsion (HPT), friction stir processing (FSP), and accumulative roll bonding (ARB) or by surface SPD, such as severe shot peening and surface mechanical attrition treatment (SMAT).[16]

SMAT is a more recent SPD process that can induce surface nanocrystallization and offers numerous advantages over other SPD processes. SMAT has the potential for simultaneously enhancing the mechanical and biological responses, similar to the bulk SPD process, with the added advantage of higher efficiency of nanocrystallization and ease of the process.[17–20] SMAT is, thus, an appealing processing technique for surface modification of implants on an industrial scale and amenable to processing of the near-net-shaped parts prepared by AM, unlike bulk SPD. Despite its many advantages, processing by SMAT has not yet been leveraged for biomedical implants, particularly for additively manufactured parts. Therefore, the goal of this study was to critically assess SMAT as means to enhance the electrochemical properties, biomechanical performance, including tribo-corrosion resistance, and biological performance, both cytocompatibility *in vitro* and biocompatibility *in vivo*. The changes to the surface microstructure, roughness, oxide layer composition, and mechanical properties induced by SMAT were characterized to elucidate the observed changes in the performance metrics.

2. Materials and methods

2.1 Fabrication of SS samples

316L SS was fabricated through a commercial contract (Intech DMLS Pvt. Ltd, Bangalore, India) by SLM (EOSINT M 280) with a 195 W power laser at a scan speed of 650 mm/s, as reported recently. The size of the powder particles varied between 25 to 50 μm. The scan strategy used in printing is shown schematically in Fig. 1a to yield dense parts with minimal defects. Each

layer was subdivided into parallel rectangular strips for processing using a bidirectional scanning strategy. The subsequent layer was printed in the same manner but was rotated 67° with respect to the underlying layer, as shown in Fig. 1a. Rectangular cuboid shape geometries were processed, as shown in Fig. 1a. Z-axis is parallel to the build direction (BD), and the X and Y axes lie in the processed layer, as represented in Fig. 1a. The relative density of the 3D printed SS 316L was 98.3%, as determined using the Archimedes principle, in agreement with our earlier work.[20]

Samples of various dimensions for different studies were wire cut by an electric discharge machine (EDM, Accutex). All the samples were machined in the horizontal orientation. Square samples (surface area 7 × 7 mm^2 and 1 mm thickness) were prepared towards the XY plane for *in vitro* cell studies; flat dog-bone-shaped samples (gauge length of 10 mm, gage width 5 mm, and thickness 2 mm) for fatigue tests (loading along the Z axis); and circular discs (5 mm diameter × 1 mm thickness) along the XY plane for *in vivo* study.

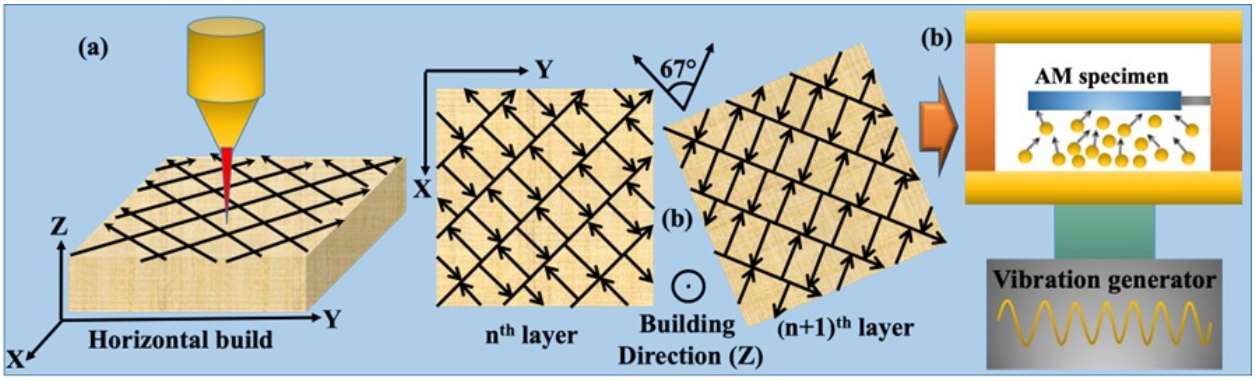

Fig. 1. Schematic of the (a) scanning strategy and (b) SMAT process.

Prior to SMAT, all the samples were mechanically polished up to 3000 grit emery paper, followed by electropolishing. SMAT was conducted at a frequency of 30 Hz with 4.75 mm hardened steel balls of hardness 50 HRC for a duration of 15 to 60 min. The SMAT unit (Fig. 1b)

was fabricated by Cosmic Industrial Laboratories Limited, Bengaluru, India, and consists of a cylindrical chamber of 170 mm diameter.[21] A total of 500 balls were used, and the distance between the specimen surface and the base of the chamber was fixed at 20 mm.

2.2 Microstructural characterization

The microstructure of the alloy was analyzed by scanning electron microscopy (SEM, Sirion, FEI) and transmission electron microscopy (TEM, FEI Tecnai F-30). Samples for SEM were prepared using standard metallographic techniques followed by etching in nital reagent. To prepare the sample for TEM, the cross-sectional lamella was sectioned out from the surface up to a depth of ≈ 6 μm by focused ion beam milling using Gallium ions at 30 kV, followed by lower-current thinning.

2.3 Surface characterization

The surface roughness of the as-manufactured alloy, after electropolishing and after SMAT, was characterized using a noncontact optical profiler (TalySurf CCI). Measurements were performed in triplicates for each sample. The thin oxide film formed on the alloy surface was characterized by X-ray photoelectron spectroscopy (XPS). High-resolution XPS spectra (narrow profiles) of Fe, Cr, and O were recorded at the outermost surface and at a depth from the surface after ion etching with Ar for 120 s, using a monochromatic Al source (1.486KeV, Kratos Analytical instruments).

2.4 Electrochemical behavior

The corrosion behavior of the alloy in the different conditions was examined by Tafel extrapolation and electrochemical impedance spectroscopy (EIS) in a simulated body fluid (SBF) solution, which was prepared as described in the literature.[21] The samples were subjected to

ultrasonic cleaning before the tests. A standard three-electrode potentiostat (CHI604E, C.H. Instruments) was used with Pt as the counter electrode and a saturated calomel electrode (SCE) as the reference. The samples were immersed in SBF for 3 h prior to polarization to stabilize the resting potential (open circuit potential, OCP). The Tafel plots were obtained at a scan rate of 12 mV/min from −600 mV to +400 mV with respect to OCP. These plots were used to calculate the corrosion potential (E_{corr}) and corrosion current density (I_{corr}) by the Tafel extrapolation technique. The EIS spectra were measured at OCP using a sinusoidal signal with 5 mV amplitude in the frequency range 10^5 to 10^{-1} Hz.

2.5. Fretting wear

The effect of SMAT on friction and wear performance was evaluated using a ball-on-plate fretting wear measurement machine (Ducom, India). ZrO_2 balls of 6 mm diameter were subjected to reciprocating motion against the XY surfaces of the rectangular cuboid samples (10×10 mm^2). The whole contact surfaces were immersed in a 20% fetal bovine serum (FBS) solution (pH=7.4) during the test. The relative displacement stroke (l) and load (PN) between the ball and sample were fixed at 5 N and ± 100 μm, respectively, and during each test. The temperature was controlled at 37 ± 2°C during each test. All the tests were performed at a frequency of 10 Hz up to 50,000 cycles. The load and stroke length chosen in the current study correspond to the gross-slip regime condition. After the test, the worn surfaces were characterized with an SEM.

2.6. Cell attachment and proliferation

Cell viability was assessed using mouse calvarial MC3T3-E1 subclone 4 pre-osteoblast cells (ATCC, USA). The MC3T3 cells were cultured in α-minimum essential medium (α-MEM, Sigma) with 10% (v/v) fetal bovine serum (FBS, Gibco) and supplemented with 1% glutamax

(Gibco) and 1% antibiotic and antimycotic mixture of penicillin−streptomycin (Sigma). The cells were cultured at 37 °C in a 5% CO_2 atmosphere in a humidified incubator. The growth medium was refreshed every 48 hours until cells reached 80% confluency. 0.25% Trypsin-0.5 mM EDTA (Gibco) was used to passage the cell. The cut samples were polished up to a finish of 0.3 µm with p3000 paper, followed by electropolishing. The polished samples were sterilized by immersing them in 70 % ethanol for 30 min, followed by exposure to UV light for 1 h. These sterile samples were placed individually in a 48 well plate. 5×10^3 MC3T3 cells were seeded on each sample along with 400 µL of culture media. As-manufactured samples were used as a control.

2.6.1 Cell proliferation

Cell viability and proliferation were evaluated using Alamar Blue assay (Sigma) on days 1, 4, and 7. The culture medium was removed, and samples were washed with PBS. 400 µL of culture media was added to each well containing 10% working solution of Alamar blue reagent (0.15 mg/mL) and incubated for 4 h at 37 °C in a CO_2 incubator. The fluorescence intensity of the solution was measured using a microplate reader (Biotek) at 530 nm excitation and 590 nm emission. The measurement for the assay was performed in quadruplicates, and data are presented as mean ± standard deviation (S.D.) for n = 4. The data obtained from the assay were subjected to statistical analyses using one-way analysis of variance (ANOVA) with Tukey's test. The differences were considered significant at $p < 0.05$.

2.6.2 Cell morphology

The morphology of cells on the samples was analyzed by fluorescence imaging. On days 1, 4, and 7, cells were fixed using 3.7 % formaldehyde solution for 30 min at room temperature. Cells were permeabilized using 0.2 % Triton X-100 (Sigma). The actin filaments were stained using

Alexa Fluor 488 (Invitrogen) at 25 µg/ml for 30 min, whereas the nuclei were stained using 0.2 µg/ml DAPI (Invitrogen) for 5 min at room temperature. The stained cells were imaged using an epi-fluorescence microscope (Olympus IX-53).

2.7 Animals study

Animal studies were performed to evaluate the immune response and corrosion pitting *in vivo* of the alloy in cranial defects (5 mm diameter; 1 mm thickness). The results of the alloy after SMAT were compared with the as-manufactured samples, untreated critical-sized cranial defect (CSD), and sham surgery. The animal experiments were approved by the Institutional Animal Ethics Committee (IAEC) and were in accordance with the guidelines of the Committee for the Purpose of Control and Supervision of Experiments on Animals (CPCSEA), Government of India. 8 weeks old male Wistar rats with a bodyweight of 300 ± 10 g were obtained from Central Animal Facility, Indian Institute of Science, Bangalore. The animals were housed in the cleanroom facility maintained under a regulated light and dark (12:12 h) schedule with free access to standard diet and drinking water. A standard protocol was followed with n = 6 number of animals in each experimental group. The rats were randomly divided into two groups for two study periods (4 and 8 weeks, n = 6). Further, rats in each group were randomly assigned to different experimental groups based on the treatment received (Right/Left) as follows: i) SMAT/CSD, ii) AM/CSD, iii) SMAT/AM, and iv) Sham. Untreated CSD of 5 mm diameter served as the negative control.

2.7.1 Surgical Procedure

All the surgeries were performed under general anesthesia by intraperitoneal injection of an anesthetic mixture: Ketamine (80 mg/kg body weight) and Xylazine (15 mg/kg body weight). Before the surgery, an ocular lubricant (Lacrigel) was applied to both eyes to prevent dryness, and

the calvarial region was shaved. Subsequently, a midline sagittal incision was extended from the occipital region using a scalpel, and bilateral cranial bone defects (diameter of 5 mm) were created using a drilling bur (Marathon micro motor drill machine). Thereafter, the implants were placed in the defect site, and the skin was sutured back (Fig. 2). Immediately after the surgery, Buprenorphine (5 mg/kg) and 0.9% saline (5 mL/kg) were administered subcutaneously for pain management and hydration, respectively. For 3 days post-surgery, all the animals were caged individually and received analgesic Buprenorphine (5 mg/kg) and antibiotic Enrofloxacin (5 mg/kg) subcutaneously. General health, behavior, and normalcy in wound healing were documented daily. After 4 and 8 weeks, the animals were sacrificed in a carbon dioxide chamber, and tissue was excised for histological examination. The biopsy (the implantation site and the adjacent tissue) obtained was fixed in 10% formalin. Before decalcifying the samples in 5% nitric acid, the metal implants were retrieved and gold-coated for examination under SEM. Further, the tissue samples were paraffin-embedded, sectioned, and stained with hematoxylin−eosin (H&E).

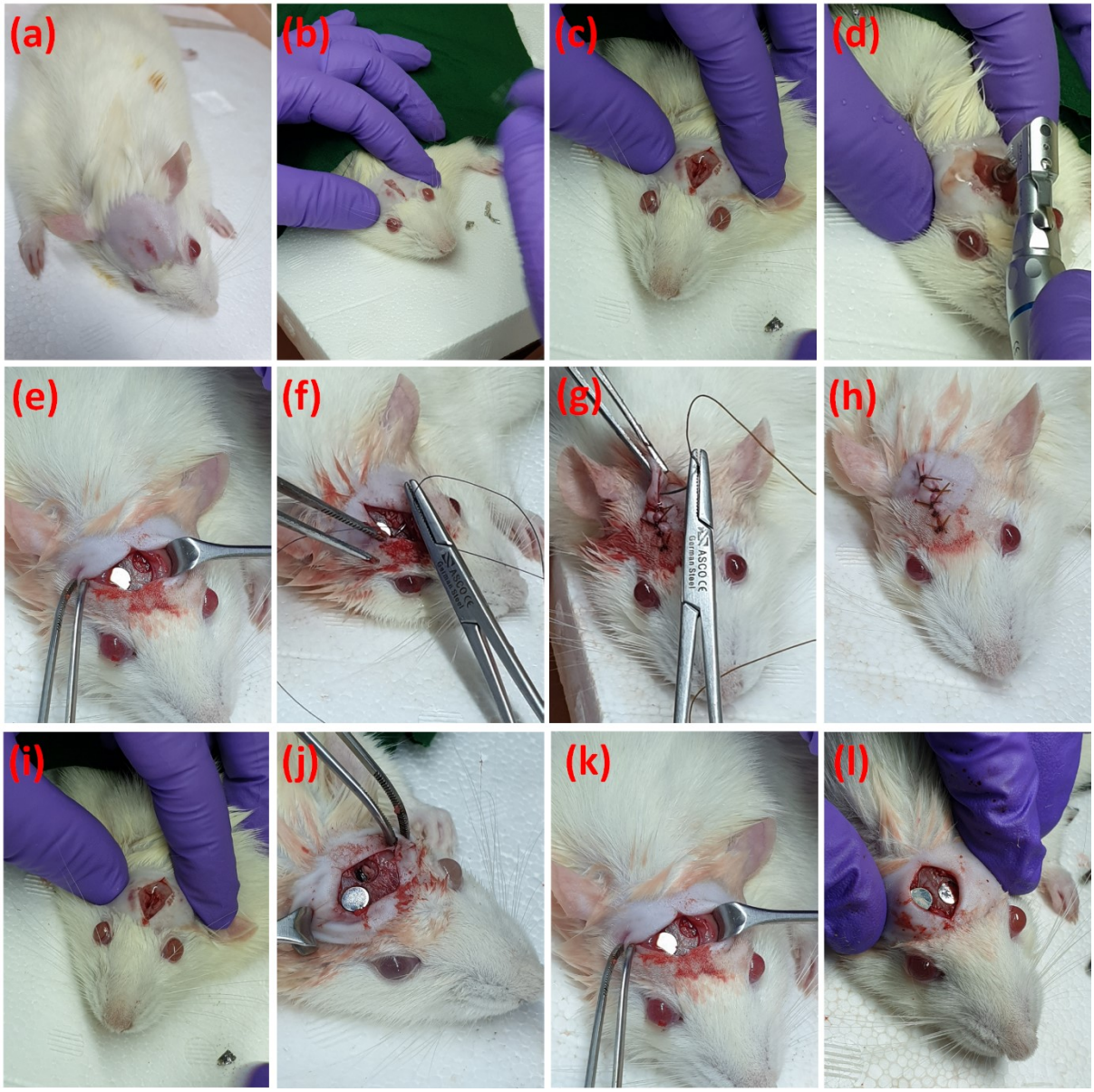

Fig. 2. The sequential steps in the surgical procedure shown from (a) to (h); Representative digital images of the different groups, i.e., Sham (i), CSD and AM implanted (j), CSD and SMAT implanted (k), AM and SMAT implanted (l) rats.

3. Results and discussion

3.1 Microstructure

Materials subjected to surface SPD exhibit graded microstructural features that progressively vary with depth, starting from the surface into the bulk. These changes induced by SMAT alter the mechanical, electrochemical, and electronic properties of the surface. The changes in the surface and bulk properties can profoundly alter the performance metrics of the biomaterial for applications in orthopedic, oral, and craniomaxillofacial applications, including fatigue, wear, and biocompatibility, among others. Therefore, the microstructural features of the as-fabricated (AM) and surface-modified (SMAT) samples were examined with an SEM (Fig. 3(a-f)) along the Y-Z plane. Fig. 3a revealed the cross-sectional view of melt pools of AM specimens with a width and depth of about 100 and 45 μm, respectively. Fine cellular substructures with two different morphologies (elongated and spherical) are observed at higher magnification (Fig. 3(b-d)). The elongated intragranular cells were ≈ 1 μm in diameter and a few micrometers in length (Fig. 3b), whereas the spherical intragranular cells had a diameter of ≈ 0.5 μm (Fig. 3c). The formation of cell structures is characteristic of 316L SS prepared by SLM and is attributed to the rapid local melting and solidification experienced during SLM. [22–24] Cells appear to be spherical or elongated depending on their growth direction with respect to the metallographic section and the direction of the temperature gradient.[22–24] The cell boundaries appear brighter than the matrix, indicating possible enrichment by heavier elements such as Cr, Mo, Ni, etc.[22–24] Fig. 3(e,f) shows the cross-section image of SMAT-15 and SMAT-60 specimens, respectively. The formation of a high density of etch pits at depths of ≈25-35 μm from the treated surfaces in both cases of SMAT-15 and SMAT-60 specimens (Fig. 3 (e, f)) is likely due to the generation of surface defects after SMAT treatment. These defects (heavily strained regions) cause the nucleation of pits after etching.

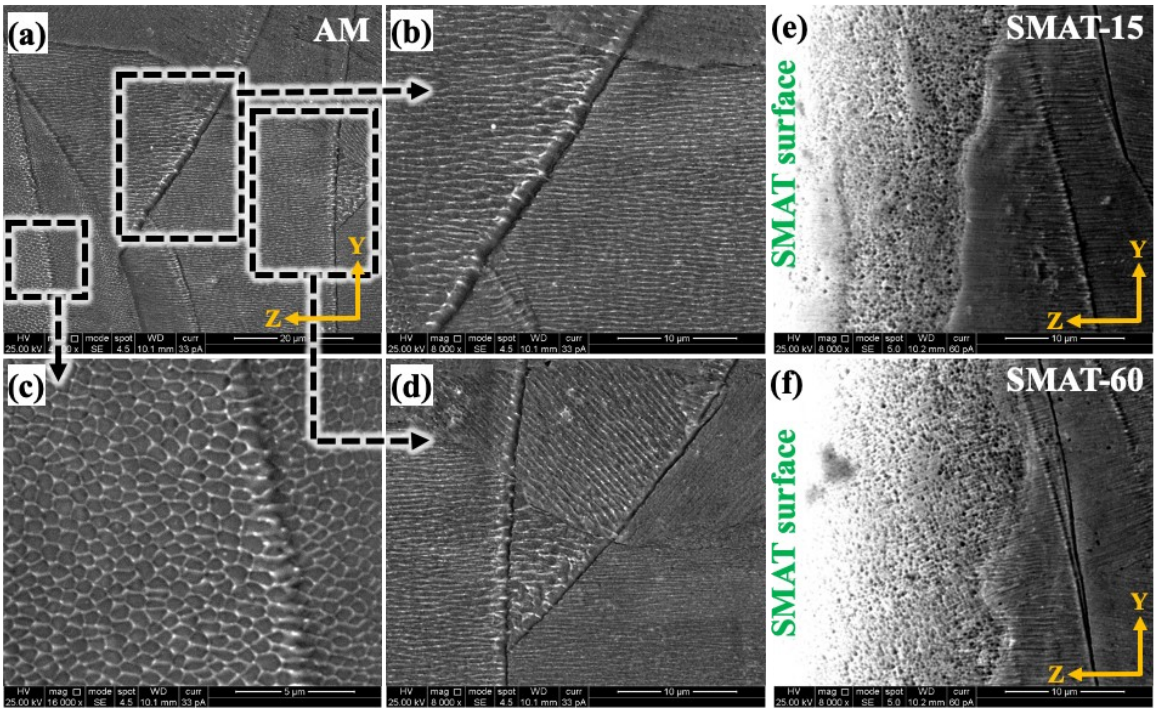

Fig. 3. (a-d) SEM images of the cross-sectional views of horizontal build AM, © SMAT-15 and (f) SMAT-60 samples.

The cell boundaries of the AM and SMAT samples were further investigated using a TEM. The bright field micrographs of the AM sample (Fig. 4a) reveal unique dislocation network structures/dislocation cells embedded within a coarse grain matrix. The selected area diffraction pattern of the corresponding area shows the characteristic spot diffraction pattern of FCC crystal structure. The high-angle annular dark-field (HAADF) scanning TEM (STEM) image of the same location shows elemental segregation adjacent to dislocation cells/network. The enrichment of Mo, Mn, Cr, and Ni along the cell boundaries was quantified by STEM-EDS analysis. The existence of spherical shape nanosized (20-90 nm) oxide particles was also revealed adjacent to the cell boundaries. The formation of dislocation cells along with segregation of the alloying elements is due to the cellular growth under the high-temperature gradient and high growth rate in SLM.

Additionally, orientation differences between the two growing neighboring cells can cause the formation of dense dislocation walls. Meanwhile, the solidification front rejects the alloying elements into the liquid phase leading to a higher content of alloying elements at the later solidified region – the cell boundaries.[25] The powders used for SLM are manufactured by gas atomization, which increases oxygen contamination and forms oxide due to its low solubility in alloys.[26]

The cross-sectional TEM bright field image of SMAT-60 is presented in Fig. 4c. The TEM image at the surface of SMAT-60 shows a nanocrystalline grain structure (Fig. 4c) together with dense dislocation substructures. The spotty ring-like selected area diffraction pattern (SADP) (inset Fig. 4d) confirms the formation of highly refined nanostructured grains adjacent to the top surface. It was also observed that the region closer to the surface exhibits high dislocation density as it has undergone the most intense plastic deformation. As described above, SLM of 316L SS generates fine cellular microstructure (Fig. 4a). These cells consist of a complex network of dislocations associated with the segregation of alloying elements (Mn, Cr, Ni, etc.) at cell boundaries due to cellular growth under the high-temperature gradient and high growth rate condition.[27] These complex networks of dislocations, along with the segregation of alloying elements, act as flexible interfaces during deformation that significantly influence dislocation behavior. These dislocation network boundaries serve as filters or soft barriers to slow down the dislocation motion during plastic deformation.[27] Due to the intense plastic deformation in 316L SS prepared by SLM when subjected to SMAT, the formation of a clear gradient dislocation structure was observed from surface to bulk (Fig. 4c). This observation inferred that dislocations are not entirely stopped by the cell walls but permitted to pass through the cell walls.

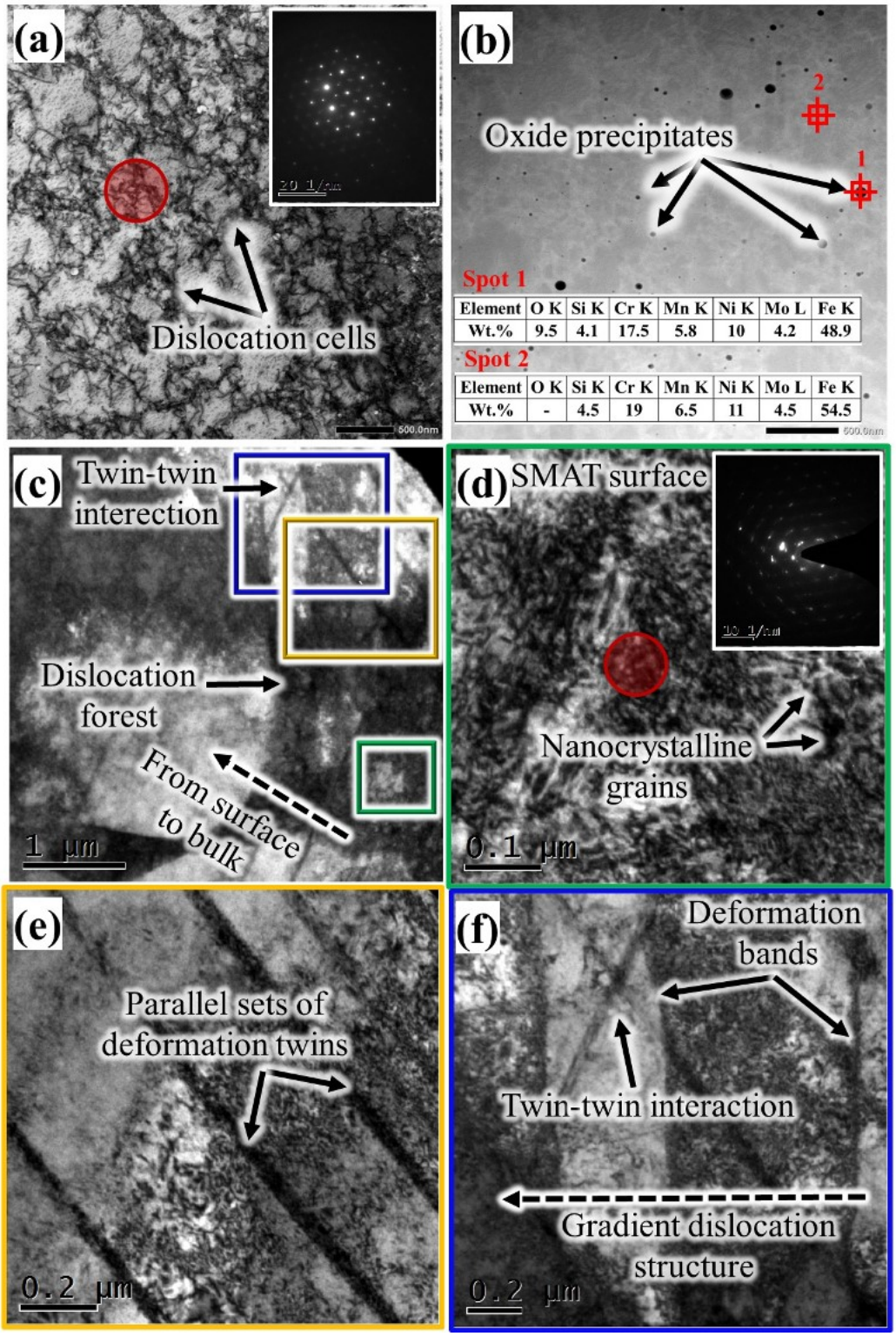
(a)
Dislocation cells
(b)
Oxide precipitates
2
1
Spot 1
Element | O K | Si K | Cr K | Mn K | Ni K | Mo L | Fe K
Wt.% | 9.5 | 4.1 | 17.5 | 5.8 | 10 | 4.2 | 48.9
Spot 2
Element | O K | Si K | Cr K | Mn K | Ni K | Mo L | Fe K
Wt.% | - | 4.5 | 19 | 6.5 | 11 | 4.5 | 54.5
(c)
Twin-twin interection
Dislocation forest
From surface to bulk
1 μm
(d)
SMAT surface
Nanocrystalline grains
0.1 μm
(e)
Parallel sets of deformation twins
0.2 μm
(f)
Deformation bands
Twin-twin interaction
Gradient dislocation structure
0.2 μm

Fig. 4. (a) Bright-field TEM micrograph of the as-manufactured alloy, inset shows the diffraction pattern of that area, (b) HAADF-STEM image of the corresponding location, (c) Bright-field TEM image of the region adjacent to the top surface layer of SMAT sample, (d) Bright field TEM micrograph of the SMAT surface; inset shows the diffraction pattern from the top surface layer, (e, f) Magnified view of selected location as marked in (c).

Apart from high dislocation density, Fig. 4c also reveals the presence of parallel sets of deformation twins at 1 μm depth from the SMAT surface (Fig. 4c). Fig. 4 (e, f) represents higher magnification micrographs of the selected region in Fig. 4c. Extremely thin deformation twins (≈50 nm thickness) were seen with increasing the depth from surface (Fig. 4e). Two different sets of twin systems can be seen to be interacting together (Fig. 4f). These twin-twin interactions act as potential sites for locking the dislocation movements in the alloy when subjected to SMAT. Gradient distribution of dislocation from surface to bulk exists in Fig. 4f. Prolonged SMAT processing facilitates the initiation and/or interactions of different deformation twins in different directions. With further increase in the strain, twin-twin intersections occur, which may split up the original matrix grains into refined blocks. This mechanism of surface nanocrystallization was proposed in our recent work on the evolution on the evolution of the surface nanocrystalline structure.[20] Notably, SPD of bulk metals is associated with dislocation-twin boundary interactions, which induces nanocrystallization.[28]

3.2 Surface characteristics

The effect of SMAT on surface characteristics was studied as they are key determinants of several vital performance parameters of a biomaterial. The 3D surface profiles of AM, AM-

electropolished, SMAT-15, and SMAT-60 surfaces characterized using a noncontact optical profiler are compiled in Fig. 5 (a-d), wherein AM-electropolished refers to the alloy after electropolishing prior to SMAT. High surface roughness (Ra = 8510 nm) was observed in the case of AM (Fig. 5a), which sharply decreased (Ra = 49 nm) after electropolishing (Fig. 5b). The Ra values for as-AM samples are close to values reported in the literature.[29] The lower Ra value in the electropolished sample is in the characteristic range of the mirror-finished sample.[29] SMAT of the electropolished samples results in increased Ra values (Fig. 5 (c,d)) due to the roughness induced by the random impact of high-energy steel balls during the treatment.[30,31] Nonetheless, the roughness values of both SMAT-15 (Ra = 796 nm) and SMAT-60 (Ra = 533 nm) were one order lower than the AM surface. This change in surface roughness depends on the processing conditions. It was observed that for a given intensity of SMAT, longer duration (SMAT-60) resulted in a smoother surface than shorter treatment (SMAT-15). The craters formed after 60 min SMAT specimen were relatively shallow and closely spaced compared to the surface features on SMAT-15. This observation further indicates that the steel balls uniformly impacted the entire surface during prolonged SMAT.

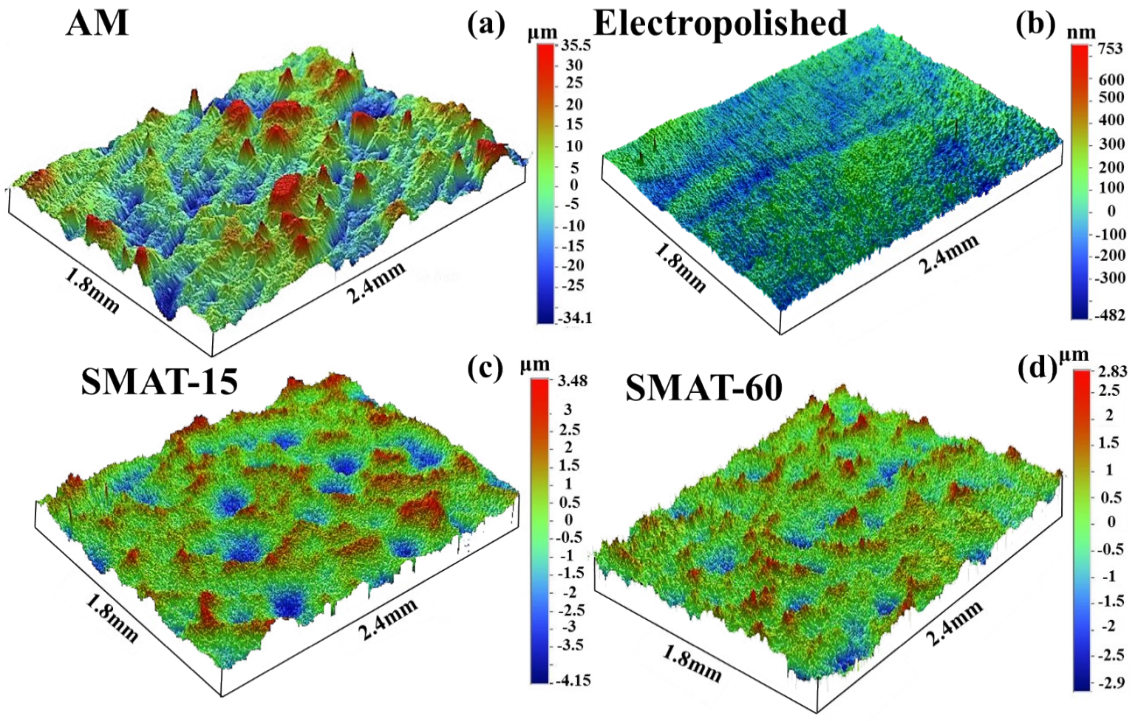

Fig. 5. The optical profilometer surface profiles at 50x for: a) AM, b) AM-Electropolished, c) SMAT-15, and d) SMAT-60 specimens.

The oxide layer formed on the surfaces was further characterized using high-resolution XPS. The spectra for Cr, Fe, and O, recorded at the surface and at a depth after 120 s of Ar etching, are compiled in Fig. 6, 7, and 8, respectively. The oxide layer is primarily composed of oxides of Fe and Cr. The oxide of Cr present in the surface layer of AM is Cr_2O_3, whereas it is a mixture of Cr_2O_3 and CrO_3 for SMAT-15 and SMAT-60. Deeper into the sample, metallic Cr was detected in AM and both the SMAT samples. The elemental quantification of the oxide layer at the outer surface and at a depth is compiled in Fig. 9. The ratio of Cr in the oxidized form to that in the metallic form was calculated by the ratio of area under the de-convoluted peaks. The ratio was the highest for SMAT-60, followed by SMAT-15 and AM (Fig. 9). This suggests that a thicker oxide

layer was formed after SMAT. Thicker oxide layers are known to augment the corrosion resistance of stainless steel.[32] The spectra for Fe revealed that the surface layer of the AM sample is primarily composed of Fe_2O_3 and a small amount of metallic Fe. The iron oxides on the SMAT surfaces are primarily FeO and Fe_2O_3, with a small amount of metallic Fe (Fig. 9). Unlike in the case of Cr, the ratio of Fe oxide to metallic Fe did not show the increase on SMAT specimens compared to AM specimen. Cr and Fe have different oxidation kinetics. Cr has a higher tendency to form a protective oxide layer (Cr_2O_3) on SMAT sample surfaces, which possibly acts as a barrier against further oxidation of Fe when the surface is subjected to the SMAT process.[33] Thus, the oxide composition changed after SMAT, from Fe rich oxide to Cr rich oxide which can explain the better oxidation resistance of SMAT compared to AM.

Oxygen is mainly present in the form of O^{2-} and OH^-. No metal hydroxides are present at the surface, which indicates that the OH peaks are likely due to adsorbed moisture.[19] Overall, these results signify that the oxide layer thickness and composition are markedly altered because of SMAT.

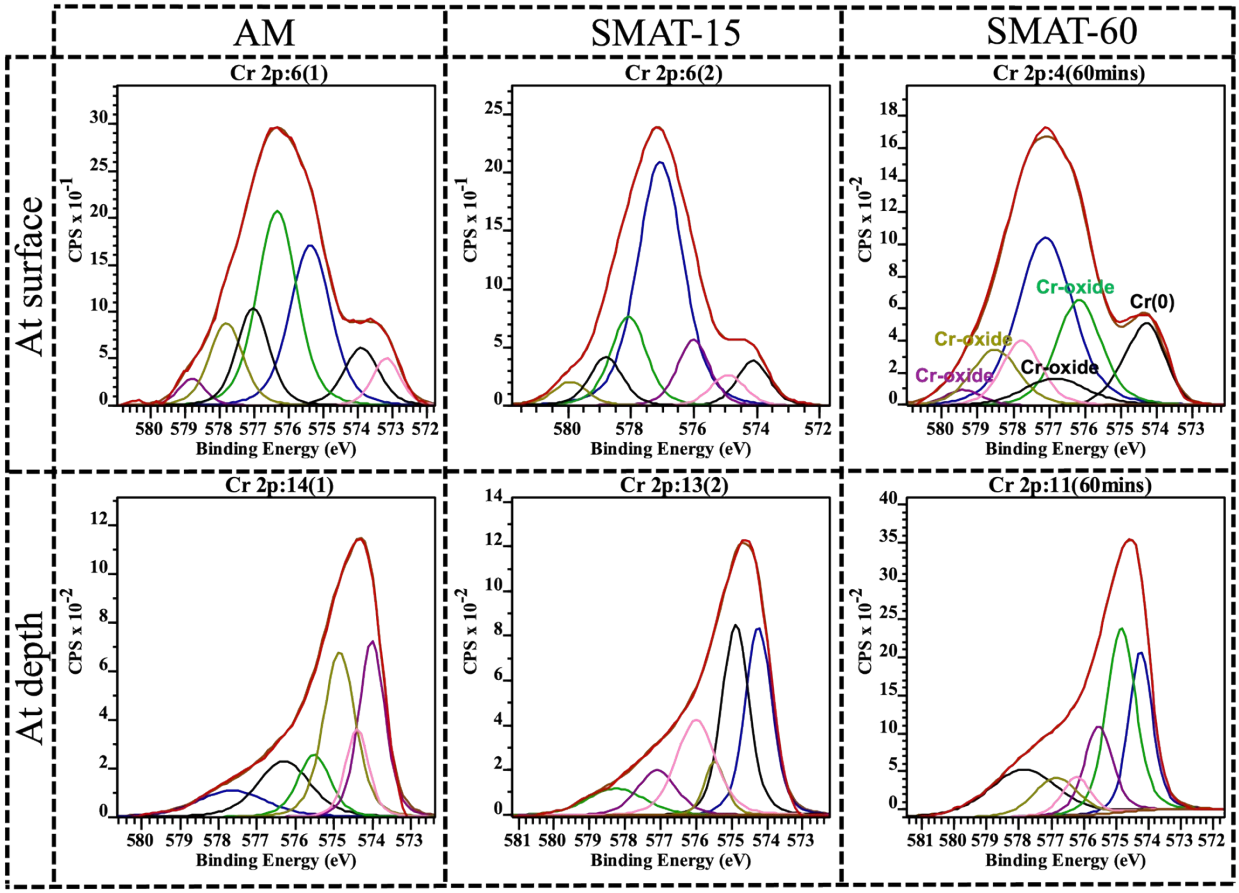

Fig. 6. High-resolution XPS spectra of Cr-2p of AM, SMAT-15, and SMAT-60 at the outer surface and at some depth following Ar etching.

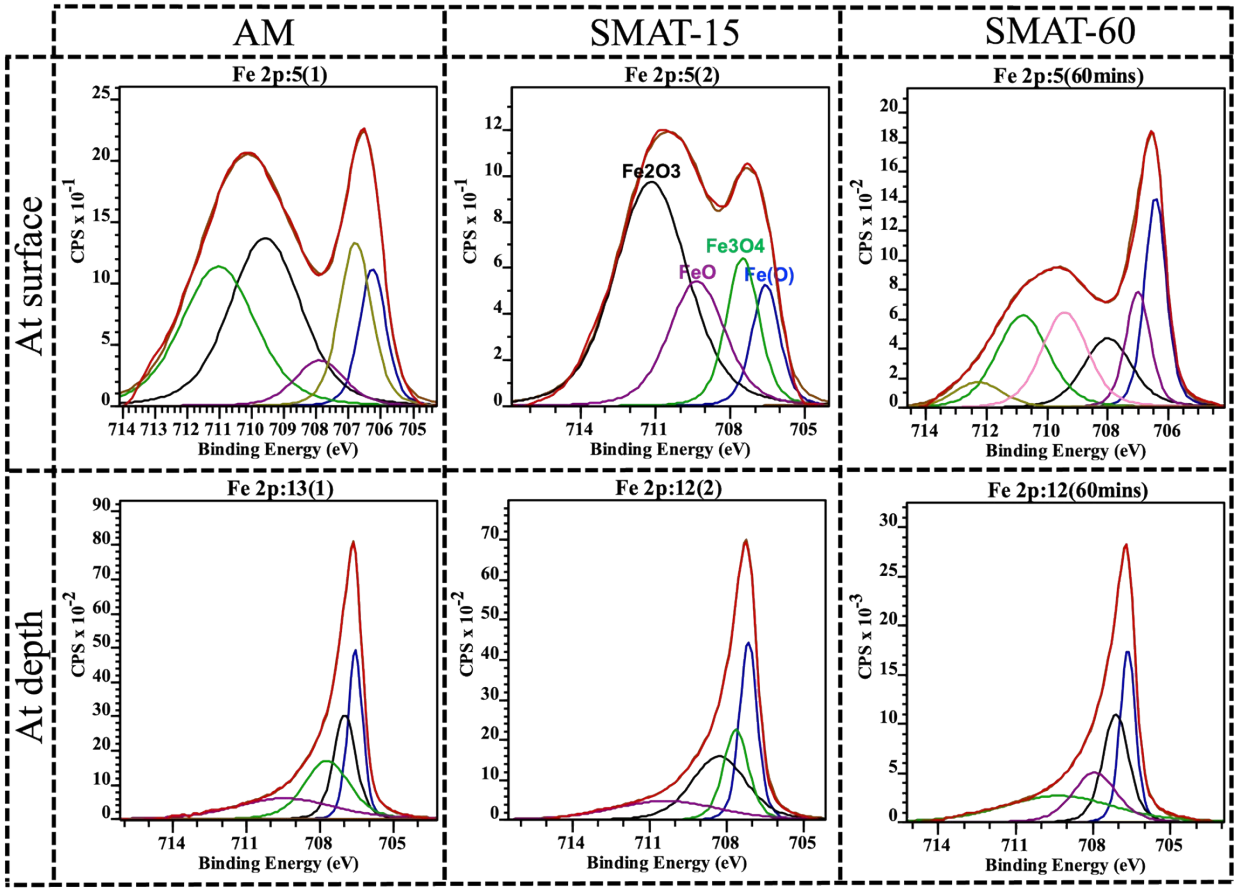

Fig. 7. High-resolution XPS scans of Fe-2p of AM, SMAT-15, and SMAT-60 at the outer surface and at some depth following Ar etching.

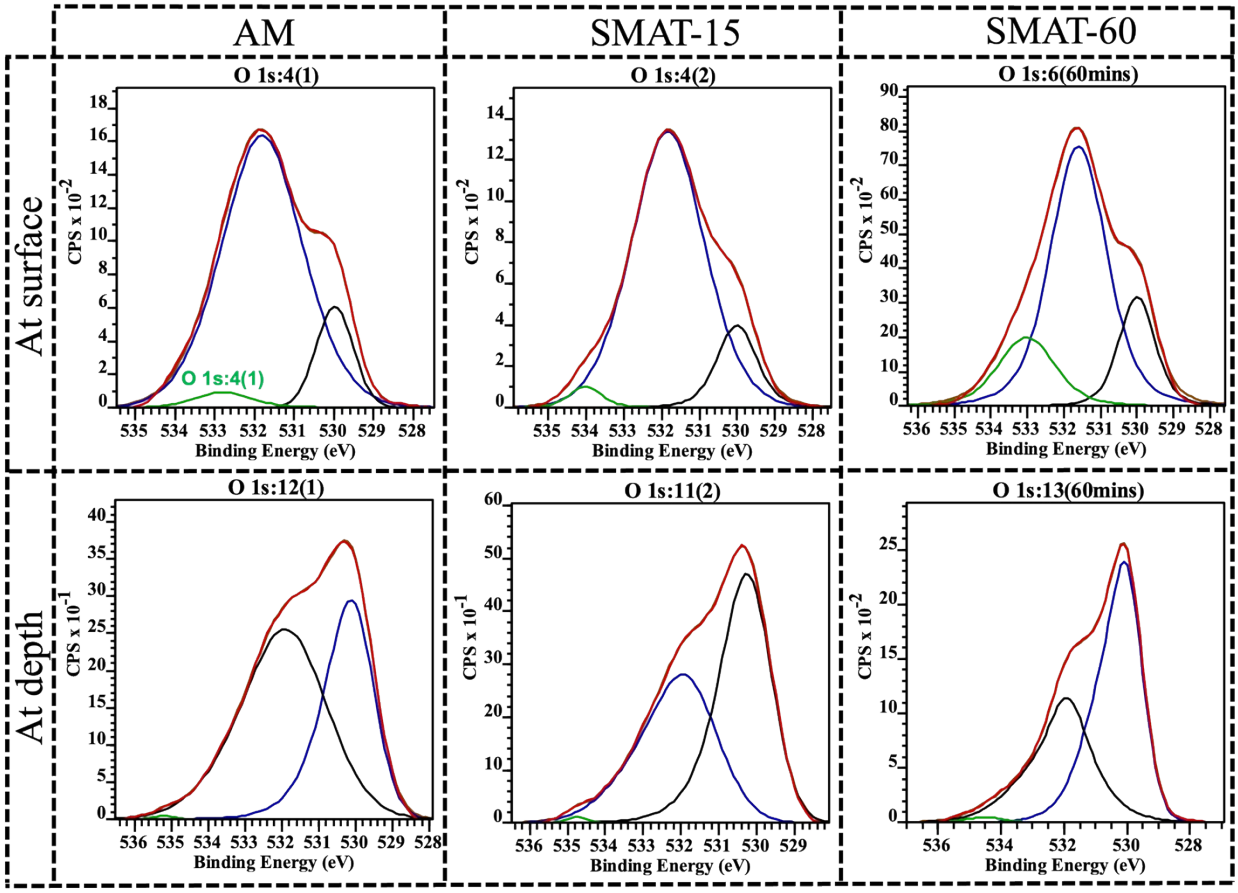

Fig. 8. High-resolution XPS scans of O-1s of AM, SMAT-15, and SMAT-60 at the outer surface and at some depth following Ar etching.

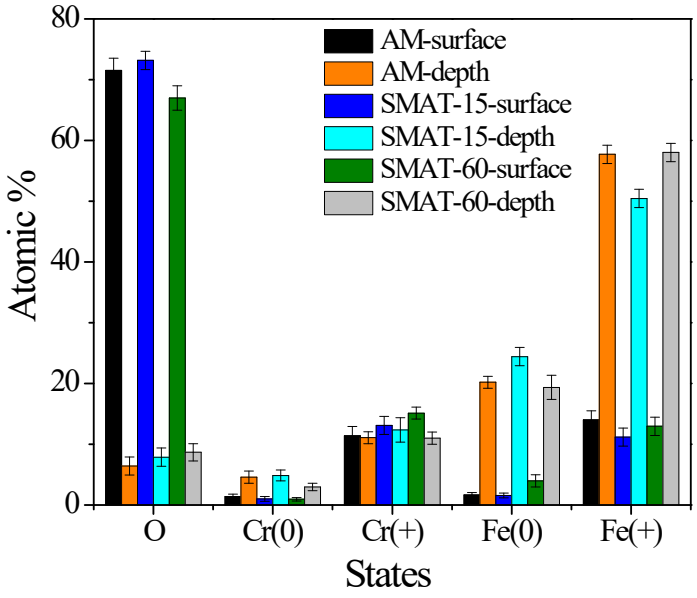

Fig. 9. Quantification of the elemental composition of the oxide layer at the outer surface and depth of AM and SMAT samples determined by analysis of XPS spectra. (+) indicates metal in the oxidized form, (0) indicates the metallic state.

3.3. Electrochemical behavior

The electrochemical behavior of AM and SMAT samples was examined by performing open circuit potential (OCP) and Tafel plot in SBF solution. For comparison, a wrought 316L SS was also used in the current study. Fig. 10a shows the open circuit potential (OCP) plots for the AM, SMAT-15, SMAT-60, and wrought 316L SS. From the OCP graph, it is observed that the potential of both AM and SMAT samples were shifted towards more positive values compared to wrought 316 L SS. Further, the potential was found to be stable throughout the OCP test, which suggests that a stable passive layer was formed on both AM and SMAT samples. However, when comparing AM and SMAT conditions, the SMAT-15 shows less stability than AM and SMAT-60 samples. Overall, it can be inferred that the stabilization of OCP was more rapid for the SMAT samples

than for AM, indicating faster passivation on the alloy when subjected to SMAT, in agreement with other studies.[32,34]

Fig. 10b presents the Tafel polarization curves of AM, SMAT-15, SMAT-60, and wrought 316L SS. The corrosion parameters, such as corrosion potential (E_{corr}), corrosion current density (I_{corr}), and passivation current density (I_{pp}), were measured and tabulated in Table 1. The Tafel polarization plot shows a mixed response. For instance, there is no significant change in the E_{corr} values for all the samples. However, I_{corr} was found to be marginally lower for wrought 316L SS compared to AM and SMAT specimens. The lower I_{corr} of wrought 316L SS might be attributed to the smooth mirror-like polished surface, whereas AM and SMAT samples possess higher surface roughness. The higher the Ra, the higher the surface area exposed to the solution, which results in higher I_{corr} values. Despite the higher I_{corr}, AM and SMAT samples at anodic potential show significantly lower I_{pp} value than wrought 316L SS. In fact, the wrought 316L SS shows no passivation behavior and the current density was found to be increasing as the potential increases. The lower I_{pp} value of AM and SMAT samples suggests that the metal dissolution was hindered at the higher potential. In other words, AM and SMAT samples tend to form a stable passive layer at the anodic region, thereby restricting the transfer of ions into the solution. When comparing AM and SMAT, though the I_{pp} value was lower for AM, instances of meta-stable pitting were observed. In marked contrast, both the SMAT 15 and SMAT 60 show no signs of meta-stable pitting in the anodic region. In addition, the SMAT 15 (at ≈0.04 V) and SMAT 60 (at ≈0.25 V) show a sudden decrease in current density, which is indicative of stable and defect-free passive layer formation. The plausible reasons for the stable and defect-free passive layer formation of SMAT samples are the SMAT-induced grain refinement and the presence of defects such as twins and dislocation array. Both grain refinement and defects increase grain boundary density. Grain boundaries are

higher energy sites and favor oxide formation.[35,36] This proposed mechanism is corroborated by the XPS results where the SMAT samples exhibit a higher ratio of Cr in the oxidized form to the metallic form in the oxide layer, further exemplifying the formation of a stable Cr_2O_3 oxide layer at the anodic potential. Finally, it can be inferred that the lower I_{pp} and the absence of meta-stable pitting of SMAT samples emphasize the importance of SPD as a favorable post-processing technique for as-printed 316L SS alloy. The mean corrosion potential (E_{corr}) is observed to increase after SMAT. An increase in E_{corr} may be ascribed to thicker oxide layer formation post-SMAT. The Tafel polarization curves (Fig. 10b) show that I_{corr} is marginally higher for AM than the wrought (conventionally processed) 316L SS, which is in agreement with other studies.[37,38] This reduced resistance is attributed to the presence of the characteristic dislocation network in AM. Dislocations and grain boundaries are high-energy sites and, hence, more susceptible to corrosion. Interestingly, I_{corr} did not increase much after SMAT compared to AM despite the formation of a defect-rich surface region. In fact, the value of Icorr was lower for SMAT-60 than for AM. The lower charge carrier density, as observed from the Tafel plots, appears to have reduced the corrosion rate.[37–40] It has been reported that SPD imparts a large number of defects in the material, leading to the formation of a stronger passive oxide on the surface.[35,36] We observed a similar trend in our earlier work following SMAT of conventionally processed 316L SS.[41] The lower charge carrier density accounts for the higher stability of the oxide layer. Thus, a simultaneous decrease in corrosion rate and critical current density for passivation is observed for the additively manufactured alloy after SMAT.

Table 1: Electrochemical parameters measured from Tafel plots.

Parameters	Wrought	AM	SMAT-15	SMAT-60
Corrosion current density, I_{corr} ($\mu A/cm^2$)	1.07	1.55	4.46	1.15
Corrosion potential, E_{corr} (V vs. SCE)	-0.250	-0.235	-0.230	-0.217
Passivation current density (I_{pp}) ($\mu A/cm^2$)	-	36.56	101.67	148.93

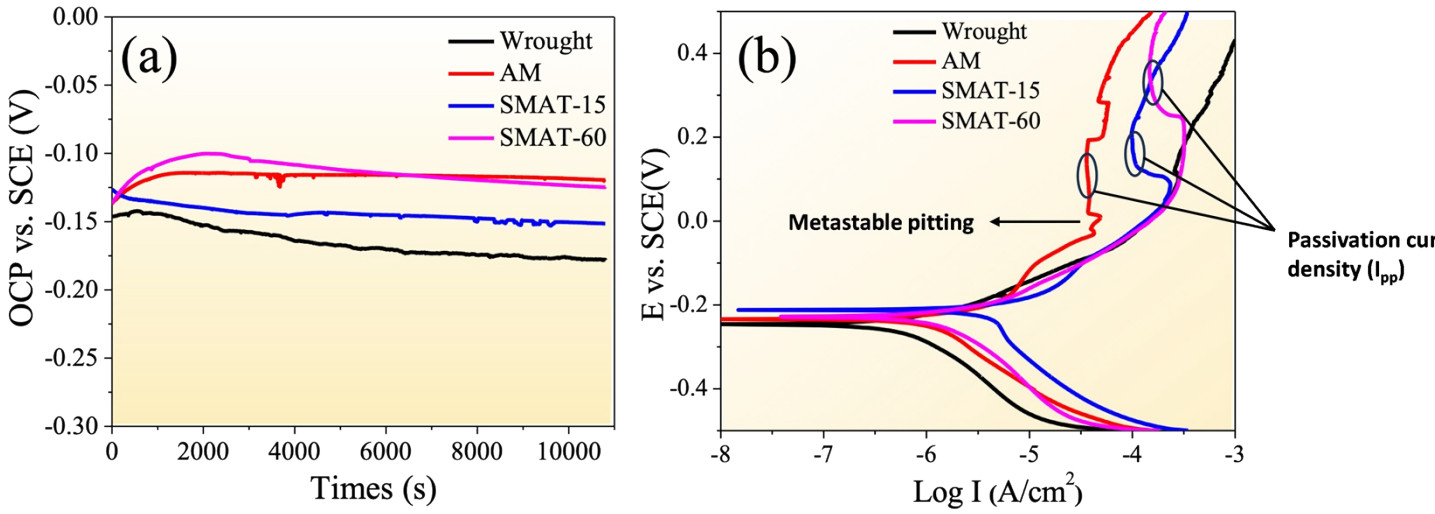

Fig. 10. a) OCP and b) Tafel plots of wrought, AM, SMAT-15, and SMAT-60 alloys.

3.4 Tribological (fretting wear) property

Load-bearing implants often experience micromotions *in vivo*, which can lead to fretting wear. Hip implants often experience fretting wear and generate wear debris, thereby resulting in aseptic loosening of implants due to adverse local tissue reactions (ALTRs).[42,43] Further, under the fretting

condition, the passive protective layer will be damaged and expose the metallic substrate to the physiological solution, which significantly affects the corrosion resistance of the components.[42] Thus, it is imperative to assess the fretting wear behavior of the implant components. In the current study, the fretting wear test was conducted for both AM and SMAT samples to understand the degradation mechanism. Fig. 11 shows the coefficient of friction (CoF) graph of both AM and SMAT specimens. The CoF graph reveals two regions: 1) short run-in wear and 2) steady state wear region. The run-in wear region corresponds to the initial higher CoF values, which were due to the presence of surface roughness. As seen from the 3D profilometer images, the AM specimen shows sharp peaks with the highest Ra value, whereas the SMAT shows a blunt peak with the formation of a crater and possesses a lower Ra. During the initial fretting motion, these peaks will be in contact with the counterpart, leading to run-in wear with higher CoF values. Despite the AM sample showing higher Ra, there is no significant change in CoF values compared to the SMAT sample in the run-in wear region. However, in the steady state region, both SMAT-15 and SMAT-60 show lower CoF than AM. This reduction in CoF might be due to the presence of craters. For instance, after the run-in wear period, most of the peaks were removed, and craters remained on the surface; these craters can act as reservoirs for the lubricant. During the fretting motion, the lubricant inside the crater tends to be drawn upwards to spread on the surface, resulting in lower CoF. In addition, the proteins in solution tend to accumulate inside the craters and restrict the direct contact of the counterpart to the substrate, leading to lower CoF. Finally, the craters also trap the wear debris formed during the run-in wear period, which hinders the third body wear.

In addition to the craters, the SMAT process produces ultra-fine grain and high dislocation density with twin formation on the surface and subsurface region, respectively. Particularly, the high dislocation density leads to a strain-hardened surface (higher surface hardness), which can

enhance the wear resistance properties of the SMAT samples, and this effect was directly reflected in the current study where the SMAT samples show lower CoF values compared to AM.[44,45]

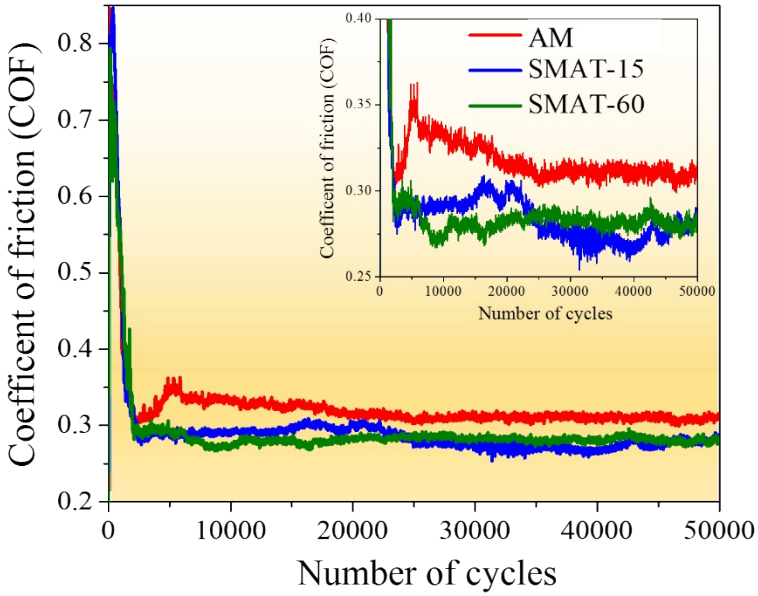

Fig. 11. Representative plots of COF vs. number of cycles up to 5×10^4 cycles of fretting wear of AM, SMAT-15, and SMAT-60.

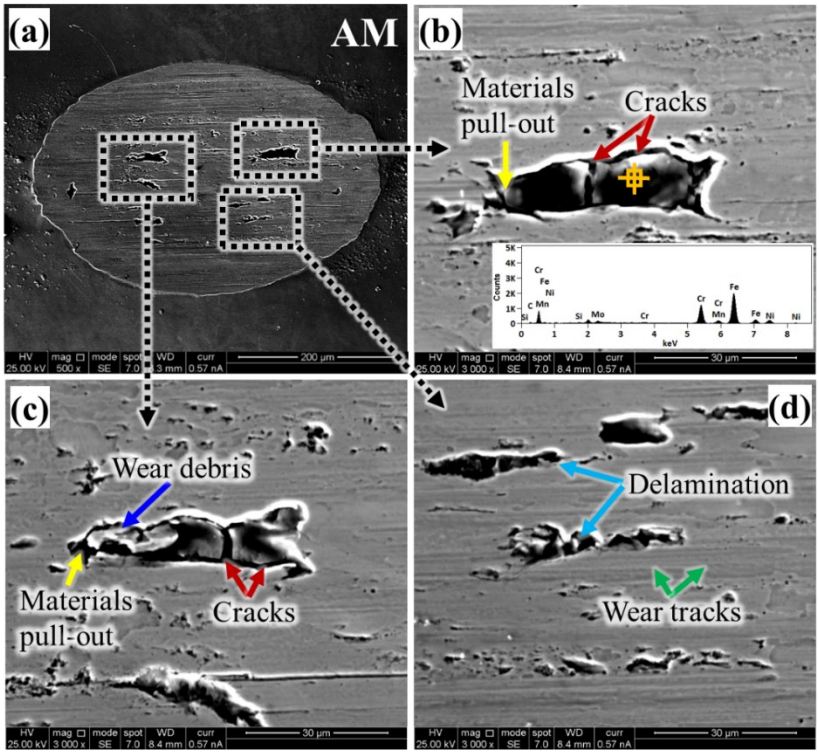

Fig. 12. Scanning electron micrographs showing the worn surface of AM.

To investigate the wear mechanism of the AM and SMAT samples, the wear tracks and debris formed after the fretting wear test were studied using an SEM in combination with EDS. Fig. 12(a-d) and 13(a-f) show the wear scars of AM and SMAT samples formed after the fretting wear test, respectively. The wear scars revealed nearly elliptical geometry in both cases, with the major axes aligned with the fretting direction. The formation of grooves and ridges towards the fretting direction inside the wear scars exhibits a typical abrasive wear activity. Additionally, material pull-out was also noticed in a few regions within wear scars. EDS spectra obtained from the particles adhered to the respective counter surfaces confirm them to be wear debris (inset Fig. 13b; and inset Fig. 13f). The size of the elliptical wear scar was the largest for AM, followed by SMAT-15 and SMAT-60. The wear scars are initiated during fretting due to continuous abrasion and indentation of the surface by the normal load aided by the electrochemical dissolution process,

eventually leading to the pull-out of worn material.[46,47] In general, the diameter of the wear scars is proportional to the depth of the wear scar, which primarily determines the amount of material removed during the process. The wear volume loss (V) is widely taken as a measure of wear rate. The approximate values of V on the surface during initial cycles by plastic deformation were calculated using the following equation.[21]

$$V = \pi R\, h^2\left(1 - \frac{h}{4R}\right)^4$$

Where R is the radius of the counterpart (ZrO_2 ball), and h is the depth of the wear scar measured by the following equation[48], where d represents the wear scar diameter.

$$h = R - \left(R^2 - {}^{d^2}/_{4}\right)^{1/2}$$

The average V values for the worn samples for AM, SMAT-15, and SMAT-60 specimens are summarized in Table 2, wherein AM shows the highest wear rate. The strain-hardening of the surface and the favorable crater formation resulted in the lower wear rate of SMAT specimens.

Table 2: Effect of SMAT on the coefficient of friction (CoF) and wear volume loss.

Condition	**CoF**	**V (x 10-3 mm3)**
AM	0.33±0.04	0.34±0.07
SMAT-15	0.29±0.06	0.23±0.03
SMAT-60	0.27±0.04	0.13±0.05

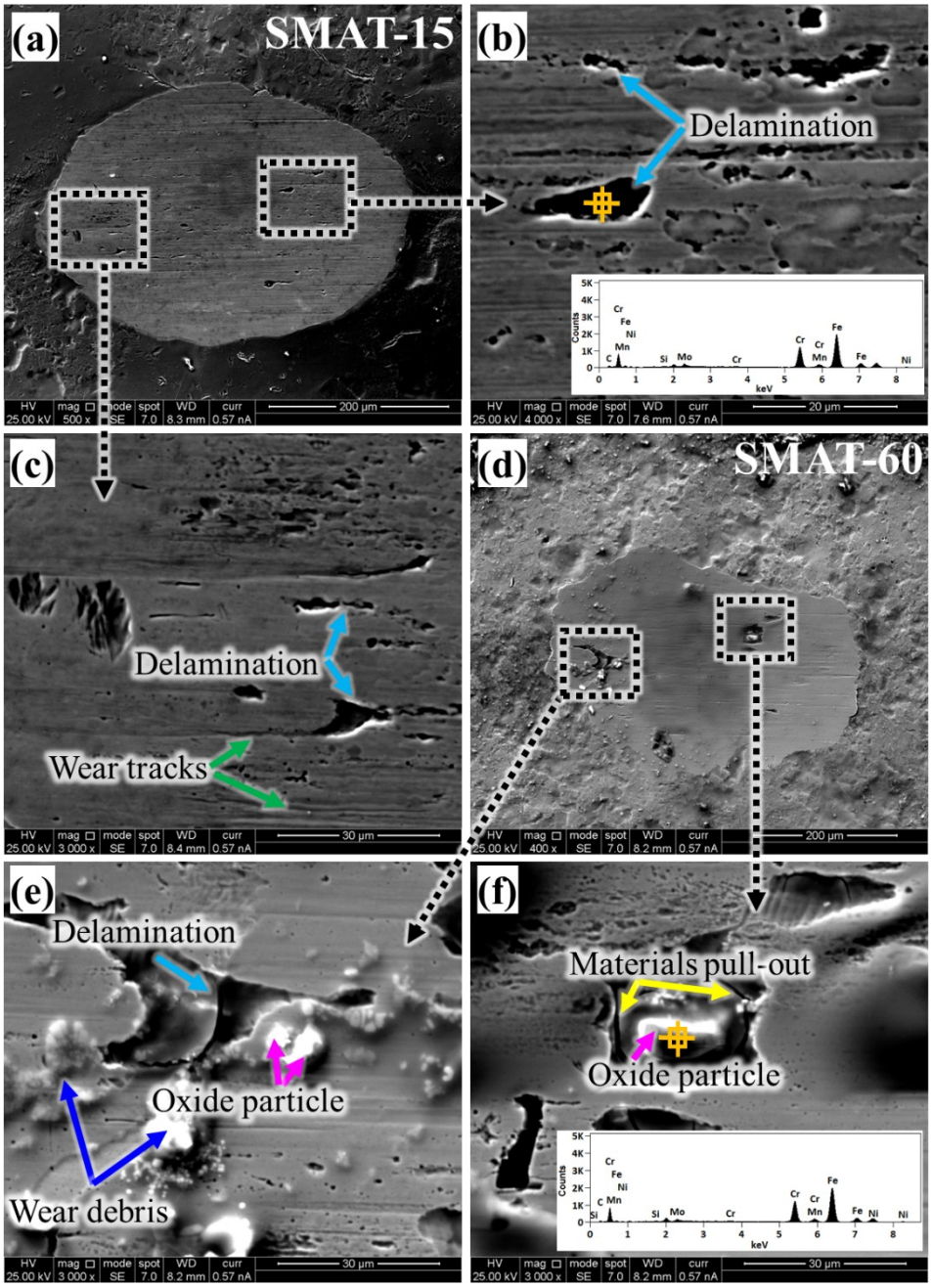

Fig. 13. Scanning electron micrographs showing the worn surface of SMAT-15 (a-c) and SMAT-60 (d-f).

3.5 Osteoblast response

As additively manufactured 316L SS are explored for orthopedic, oral, cranial, and maxillofacial devices, *in vitro* cytocompatibility tests were performed using pre-osteoblasts. Cell attachment and proliferation were assessed by measuring the metabolic activity of the cells, which is taken as a quantitative measure of viable cells (Fig. 14a). The fluorescence intensity increased from day 1 to day 4 and further to day 7 for all the samples. This result demonstrates that cells proliferated well on all samples, thereby establishing the cytocompatibility of the samples. The fluorescence intensity for the AM sample is significantly lower ($p < 0.05$) than that of SMAT-15 and SMAT-60 on day 7. Improved cell attachment and proliferation are attributed to the thicker oxide layer on the surface of the SMAT specimen. Increased charge carrier density in the oxide layer leads to easier electron transport to the electrolyte. Consequently, a net positive charge developed on the metal surface favors cell adhesion. The changes in the electronic and physicochemical properties of the oxide layer are known to modulate protein adsorption, thereby causing enhanced cell attachment and proliferation.[31] Cell attachment and proliferation were further analyzed by fluorescence imaging of cells seeded on different samples at various day points. The representative fluorescence micrographs are presented in Fig. 14b. The actin filaments are stained in green, whereas nuclei are shown in blue. The cells were evenly spread on day 1 for all the conditions, and cell numbers appear to have increased till day 7. The cells in all the conditions displayed fibroblast-like spindle-shaped morphology.

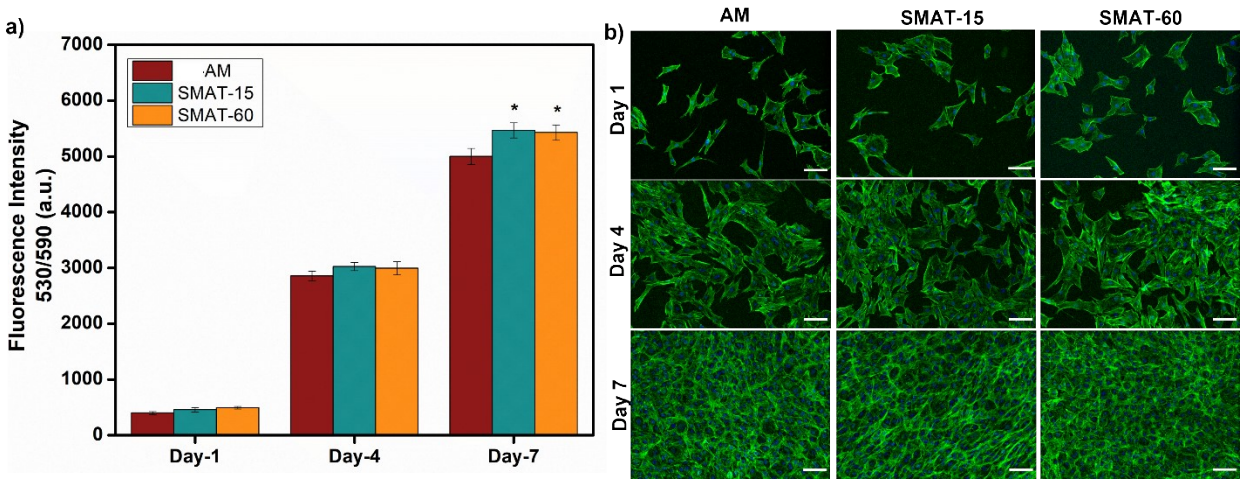

Fig. 14. a) Cell viability on AM, SMAT-15, and SMAT-60, determined by Alamar blue assay at days 1, 4, and 7. * indicates statistically significant difference compared with the control (AM) with $p < 0.05$ and $n = 4$. b) Representative fluorescent micrographs of MC3T3 cells on the surface of three types of samples at different time points, showing actin filament (green) and nuclei (blue) (scale bar = 100 μm).

3.6 *In vivo* studies

Since SMAT-60 demonstrated better fretting wear resistance, corrosion fatigue, and cellular response than SMAT-15, we selected SMAT-60 for *in vivo* investigation in a critical-sized cranial defect of a murine model. We assessed the immune response and changes in the surface characteristics of AM and SMAT-60. The results were compared with the untreated critical-sized cranial defects (CSD) and sham. Tissue biopsy was stained with H&E after 4 and 8 weeks post-surgery (Fig. 15a). No prominent differences in cellular morphology were observed across all the experimental groups. Nonetheless, moderate inflammation was observed in all the groups after 4 weeks (inflammatory cells are marked with yellow arrows), whereas no sign of inflammation was

noted after 8 weeks. These observations corroborate the findings of Marins *et al*.[49], wherein the inflammation after 1 month of surgery was attenuated after 3 months. Thus, these results indicate the additively manufactured AM 316L SS does not elicit an adverse immune response and is biocompatible. Furthermore, SMAT does not compromise the *in vivo* compatibility of the alloy. Further, the surfaces of the retrieved implants were examined with an SEM. The micrographs of AM and SMAT surfaces (Fig. 15b) reveal that neither show hallmarks of corrosion pits until 8 weeks. Notably, SMAT-60 surfaces revealed visibly enhanced interactions with the cellular components. This is in agreement with the *in vitro* results indicating enhanced cell proliferation on the surfaces following SMAT. These findings of the preliminary *in vivo* tests presented here indicate that SMAT appears as a viable strategy to favorably alter the surface properties of the additively manufactured 316L SS for enhanced bioactivity that could eventually lead to enhanced osseointegration. However, more preclinical tests are warranted to further strengthen these observations.

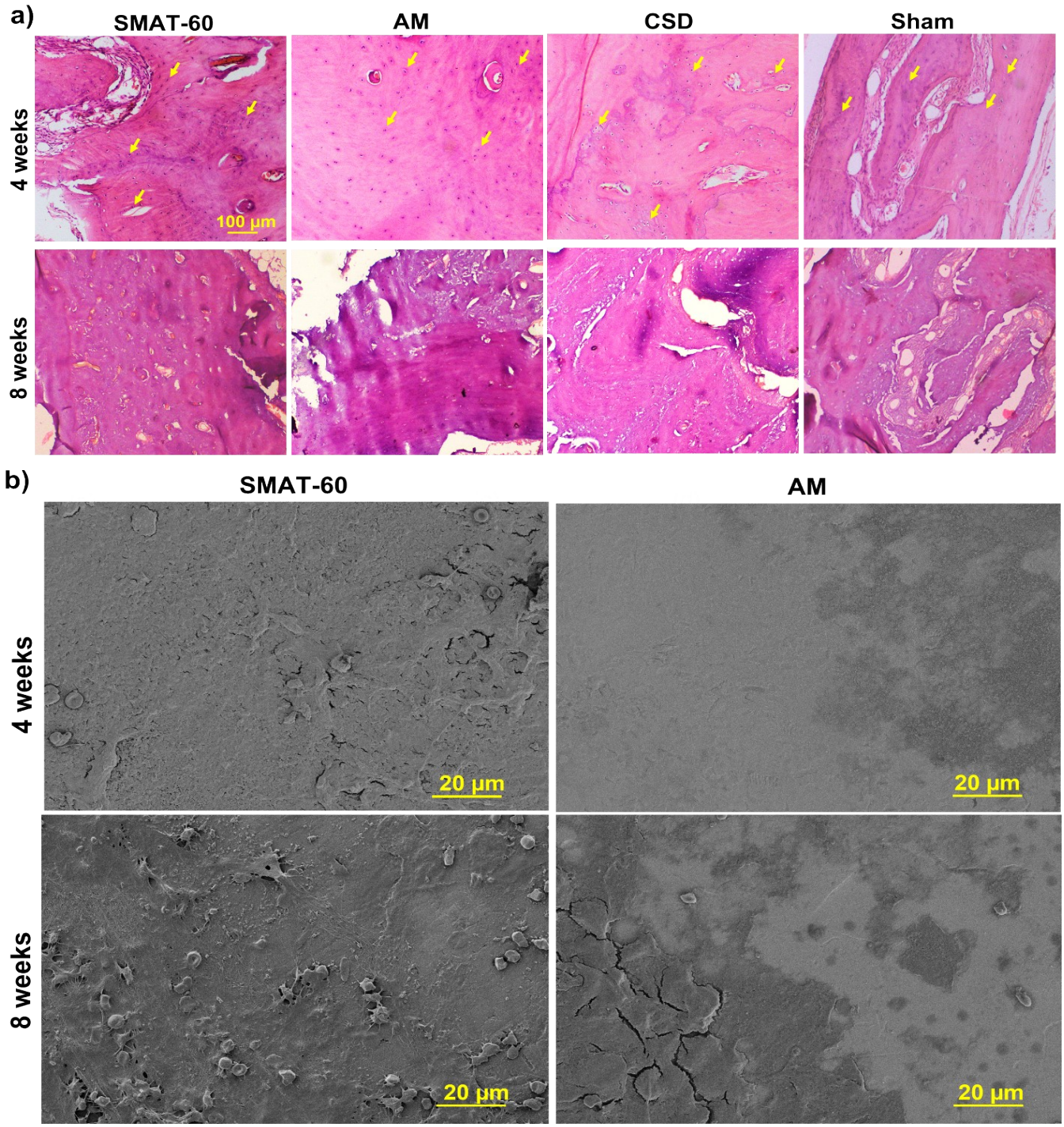

Fig. 15. a) Histological sections of decalcified tissue surrounding the implant site after 4 and 8 weeks. Yellow arrows indicate inflammatory cells. b). Scanning electron micrographs of the implant surface at 4 and 8weeks post-surgery.

The benefits of metal additive manufacturing in the biomedical industry are widely recognized. As the most mature metal additive manufacturing technology, SLM can be leveraged for the fabrication of orthopedic, oral, cranial, and maxillofacial implants of complex geometry and/or personalized to best meet the patient's needs. There is a need to develop surface engineering techniques to mitigate the limitations of the as-prepared parts for the best clinical outcomes. Although bulk SPD techniques can augment the mechanical, electrochemical, and even biological responses to metallic biomaterials, only surface SPD techniques can be used for near-net-shaped parts prepared by additive manufacturing. Surface nanostructuring offers a promising route to augment the performance of these additively manufactured implants, as demonstrated in this work. Whereas stress shielding is a concern with metallic implants, it is typically determined by the bulk elastic modulus of the biomaterial and its mismatch of the bone. For a given material, SMAT induces plastic deformation to alter the strength but is unlikely to affect the modulus since the material composition is not altered. In this work, the alloy composition and phase did not undergo any remarkable changes to markedly alter the modulus. To mitigate stress shielding, either a different alloy with intrinsically lower elastic modulus can be used or porous implants can be designed. We envisage that SMAT can be applied to other alloys or to the surface of the porous implants.

Additive manufacturing can be used to fabricate patient-specific implants of complex geometries. However, there is significant scope for improving the performance of the additively manufactured parts. As demonstrated here, SMAT offers several benefits in a manner demonstrated by the results of this work. Thus, additive manufacturing can be combined with SMAT as a post-fabrication technique to engineer high-performance next-generation medical devices. The work presented in this study demonstrates the feasibility of using SMAT to augment the performance of 316L SS

prepared by SLM. In our earlier work, we characterized the changes in the microstructure after SMAT. A gradient microstructure is generated with a hardened nanocrystalline surface that gradually changes to a microcrystalline bulk with depth. The results here demonstrate that SMAT improves the corrosion resistance of the alloy owing to the changes in the surface oxide layer characteristics. The corrosion-fatigue strength and the tribocorrosion resistance are remarkably improved. The cellular response and the *in vivo* biocompatibility were also found to be enhanced after the alloy was subjected to SMAT. Taken together, this work establishes surface modification by SMAT as a potent route of post-printing modification of additively manufactured parts to engineer high-performance next-generation medical devices.

4. Conclusion

The effect of SMAT treatment on 316L SS fabricated by SLM was systematically investigated and compared to as-fabricated additively manufactured samples to assess the effects on electrochemical, biomechanical, and biological performances. Changes in material properties of SMAT performed for different time durations (15 and 60 min) were studied. SMAT induced surface nanocrystallization, yielding a gradient in increased grain sizes from the surface to the bulk. Surface characterization with high-resolution XPS revealed a higher ratio of oxide to the metallic form of Cr and Fe in SMAT specimens. Assessment of the corrosion resistance revealed that the mean corrosion potential (E_{corr}) was higher after SMAT. The fretting wear rate measured in a corrosive environment significantly improved after SMAT due to the formation of hardened surface layers. The *in vitro* cell studies revealed a significantly higher ($p < 0.05$) cell proliferation on the SMAT surfaces than on AM. Further, *in vivo* performance of as-AM and SMAT-60 was tested in a critical-sized cranial defect of a murine model. Histological analysis confirmed that

SMAT does not induce adverse immune responses. Surface assessment of the retrieved implants showed no hallmarks of corrosion pit formation and, in fact, enhanced cellular interactions with the SMAT sample than with AM. Overall, the results establish SMAT as an excellent surface treatment route for additively manufactured components to concurrently improve several performance metrics for use in orthopedic, oral, and craniomaxillofacial implants.

Acknowledgements

This work is funded by the Department of Science and Technology (DST), Government of India (DST/NM/NB/2018/119(G)).

Conflict of Interests

The authors have no conflicts of interest to declare.

References

1 M. Navarro, A. Michiardi, O. Castaño and J. A. Planell, *J. R. Soc. Interface*, 2008, **5**, 1137–1158.

2 A. Mahapatro, *J. Biomater. Tissue Eng.*, 2012, **2**, 259–268.

3 D. Khrapov, A. Paveleva, M. Kozadayeva, S. Evsevleev, T. Mishurova, G. Bruno, R. Surmenev, A. Koptyug and M. Surmeneva, *Mater. Sci. Eng. A*, 2023, **862**, 144479.

4 S. Bahl, S. R. K. Meka, S. Suwas and K. Chatterjee, *ACS Biomater. Sci. Eng.*, 2018, **4**, 3132–3142.

5 M. Dinu, S. Franchi, V. Pruna, C. M. Cotrut, V. Secchi, M. Santi, I. Titorencu, C. Battocchio, G. Iucci and A. Vladescu, *Titan. Med. Dent. Appl.*, 2018, 175–200.

6 S. Bahl, S. Suwas and K. Chatterjee, *Int. Mater. Rev.*, 2020, **66**, 114–139.

7 S. Bahl, S. R. K. Meka, S. Suwas and K. Chatterjee, *ACS Biomater. Sci. Eng.*, 2018, **4**, 3132–3142.

8 N. Nadammal, M. Rajput, S. K. Gupta, E. Ivanov, A. S. Reddy, S. Suwas and K. Chatterjee, *ACS Omega*, 2022, **7**, 8506–8517.

9 D. Herzog, V. Seyda, E. Wycisk and C. Emmelmann, *Acta Mater.*, 2016, **117**, 371–392.

10 S. L. Sing, J. An, W. Y. Yeong and F. E. Wiria, *J. Orthop. Res.*, 2016, **34**, 369–385.

11 V. M. S. Muthaiah, S. Indrakumar, S. Suwas and K. Chatterjee, *Bioprinting*, 2022, **25**, e00180.

12 E. Yasa, J. Deckers and J. P. Kruth, *Rapid Prototyp. J.*, 2011, **17**, 312–327.

13 I. Tolosa, F. Garciandía, F. Zubiri, F. Zapirain and A. Esnaola, *Int. J. Adv. Manuf. Technol.* 2010, **51**, 639–647.

14 A. Balamurugan, S. Rajeswari, G. Balossier, A. H. S. Rebelo and J. M. F. Ferreira, *Mater. Corros.*, 2008, **59**, 855–869.

15 B. Aksakal, Ö. S. Yildirim and H. Gul, *J. Fail. Anal. Prev. 2004 43*, 2004, **4**, 17–23.

16 D. J. Alexander, *J. Mater. Eng. Perform.*, 2007, **16**, 360–374.

17 S. Acharya, S. Suwas, K. Chatterjee, *Nanoscale*, 2021, **13**, 2286–2301.

18 T. Roland, D. Retraint, K. Lu and J. Lu, *Scr. Mater.*, 2006, **54**, 1949–1954.

19 S. Bahl, P. Shreyas, M. A. Trishul, S. Suwas, K. Chatterjee, *Nanoscale*, 2015, **7**, 7704–7716.

20 S. Ghosh, N. Bibhanshu, S. Suwas, K. Chatterjee, *Mater. Sci. Eng. A,* 2021, **820**, 141540.

21 S. Acharya, A. G. Panicker, V. Gopal, S. S. Dabas, G. Manivasagam, S. Suwas, K. Chatterjee, *Mater. Sci. Eng. C*, 2020, **110**, 110729.

22 R. Casati, J. Lemke and M. Vedani, *J. Mater. Sci. Technol.*, 2016, **32**, 738–744.

23 M. L. Montero-Sistiaga, M. Godino-Martinez, K. Boschmans, J. P. Kruth, J. Van Humbeeck and K. Vanmeensel, *Addit. Manuf.*, 2018, **23**, 402–410.

24 J. Suryawanshi, K. G. Prashanth and U. Ramamurty, *Mater. Sci. Eng. A*, 2017, **696**, 113–121.

25 V. B. Vukkum, J. Christudasjustus, A. A. Darwish, S. M. Storck and R. K. Gupta, *npj Mater. Degrad. 2022 61*, 2022, **6**, 1–11.

26 X. Lou, P. L. Andresen and R. B. Rebak, *J. Nucl. Mater.*, 2018, **499**, 182–190.

27 L. Liu, Q. Ding, Y. Zhong, J. Zou, J. Wu, Y. L. Chiu, J. Li, Z. Zhang, Q. Yu and Z. Shen, *Mater. Today*, 2018, **21**, 354–361.

28 R. Valiev, *Nat. Mater. 2004 38*, 2004, **3**, 511–516.

29 P. Tyagi, T. Goulet, C. Riso and F. Garcia-Moreno, *Int. J. Adv. Manuf. Technol. 2018 1009*, 2018, **100**, 2895–2900.

30 N. Li, Y. D. Li, Y. X. Li, Y. H. Wu, Y. F. Zheng and Y. Han, *Mater. Sci. Eng. C*, 2014, **35**, 314–321.

31 S. Bahl, B. T. Aleti, S. Suwas and K. Chatterjee, *Mater. Des.*, 2018, **144**, 169–181.

32 S. Jelliti, C. Richard, D. Retraint, T. Roland, M. Chemkhi and C. Demangel, *Surf. Coatings Technol.*, 2013, **224**, 82–87.

33 L. Wang, A. Seyeux, P. Marcus, *Corr. Sci.*, 2019, **165**, 108395.

34 L. Jin, W. F. Cui, X. Song, G. Liu and L. Zhou, *Trans. Nonferrous Met. Soc. China*, 2014, **24**, 2529–2535.

35 A. A. Ahmed, M. Mhaede, M. Wollmann and L. Wagner, *Surf. Coatings Technol.*, 2014, **259**, 448–455.

36 H. Miyamoto, *Mater. Trans.*, 2016, **57**, 559–572.

37 D. J. Sprouster, W. Streit Cunningham, G. P. Halada, H. Yan, A. Pattammattel, X. Huang, D. Olds, M. Tilton, Y. S. Chu, E. Dooryhee, G. P. Manogharan and J. R. Trelewicz, *Addit. Manuf.*, 2021, **47**, 102263.

38 J. R. Trelewicz, G. P. Halada, O. K. Donaldson and G. Manogharan, *JOM*, 2016, **68**, 850–859.

39 X. Hou, Q. Ren, Y. Yang, X. Cao, J. Hu, C. Zhang, H. Deng, D. Yu, K. Li and W. Lan, *J. Nat. Gas Sci. Eng.*, 2021, **86**, 103718.

40 V. Salarvand, H. Sohrabpoor, M. A. Mohammadi, M. Nazari, R. Raghavendra, A. Mostafaei and D. Brabazon, *J. Mater. Res. Technol.*, 2022, **18**, 4104–4113.

41 S. Bahl, S. Suwas, T. Ungàr and K. Chatterjee, *Acta Mater.*, 2017, **122**, 138–151.

42 T. Yue and M. Abdel Wahab, *Tribol. Int.*, 2017, **107**, 274–282.

43 D. K. Zhang, S. R. Ge and Y. H. Qiang, *Wear*, 2003, **255**, 1233–1237.

44 M. M. Khruschov, *Wear*, 1974, **28**, 69–88.

45 J. F. Archard, *J. Appl. Phys.*, 2004, **24**, 981.

46 J. Liu, H. Dong, J. Buhagiar, C. F. Song, B. J. Yu, L. M. Qian and Z. R. Zhou, *Wear*, 2011, **271**, 1490–1496.

47 S. A. Kumar, S. K. Sai, S. G. S. Raman, R. Gnanamoorthy, *Tribo. Mater. Surf. Inter.,* 2013, **7**, 168–174.

48 A. Amanov, I.S. Cho, D.E. Kim, Y.S. Pyun, *Surf. Coatings Technol.,* 2012, **207**, 135–142.

49 L. V. Marins, T. M. Cestari, A. D. Sottovia, J. M. Granjeiro, R. Taga, *J. Appl. Oral Sci.*, 2004,**12**, 62–69.